

Subhalo abundance matching using progenitor mass

Shogo Masaki^{1,2} , Daichi Kashino^{3,2} and Yen-Ting Lin⁴

¹*National Institute of Technology, Suzuka College, Suzuka, Mie 510-0294, Japan*

²*Department of Physics, Nagoya University, Nagoya, Aichi 464-8601, Japan*

³*Institute for Advanced Research, Nagoya University, Nagoya, Aichi 464-8601, Japan*

⁴*Institute of Astronomy and Astrophysics, Academia Sinica (ASIAA), Taipei 10617, Taiwan*

Accepted XXX. Received YYY; in original form ZZZ

ABSTRACT

We propose a novel subhalo abundance matching (SHAM) model that uses the virial mass of the main progenitor of each (sub)halo M_{prog} as a proxy of the galaxy stellar mass M_* at the time of observation. This M_{prog} model predicts the two-point correlation functions depending on the choice of the epoch z_{prog} at which M_{prog} is measured. With z_{prog} as a fitting parameter, we apply the M_{prog} model to the latest observed angular correlation functions of galaxy samples at $z \simeq 0.4$ with varying stellar mass thresholds from $M_{*, \text{lim}}/(h^{-2} M_\odot) = 10^{11}$ to $10^{8.6}$. The M_{prog} model can reproduce the observations very well over the entire scale range of 0.1 – $10 h^{-1}$ Mpc. We find that, for the samples of $10^9 \leq M_{*, \text{lim}}/(h^{-2} M_\odot) \leq 10^{10.2}$, the correlation functions predicted by the widely-used V_{peak} model lacks amplitudes at the scale of $\lesssim 1 h^{-1}$ Mpc, demonstrating the high capability of our M_{prog} model to explain observed clustering measurements. The best-fit z_{prog} parameter is highest ($z_{\text{prog}} \simeq 5$) for intermediate mass galaxies at $M_* \simeq 10^{9.7} h^{-2} M_\odot$, and becomes smaller towards $z_{\text{prog}} \simeq 1$ for both lower- and higher-mass galaxies. We interpret these trends as reflecting the downsizing in the in-situ star formation in lower-mass galaxies and the larger contribution of ex-situ stellar mass growth in higher-mass galaxies.

Key words:

1 INTRODUCTION

The observed spatial distribution of galaxies contains a huge amount of physical information on cosmology, and galaxy formation and evolution. To extract such information accurately from modern wide-field galaxy surveys, it is necessary to correctly model the relations between the observed galaxies and their host dark matter structures, i.e., halos and their substructures, subhalos¹.

One of the empirical methods widely used for modeling the galaxy–subhalo connection is the subhalo abundance matching (SHAM) method (Kravtsov et al. 2004; see Wechsler & Tinker 2018 for a recent review). The SHAM method assumes a monotonic relation with some scatter between a galaxy observable and a simulated subhalo property. In the simplest form, known as the rank-ordering SHAM, for a sample of observed galaxies selected by a threshold in some physical property (e.g., stellar mass or luminosity), the corresponding subhalo sample is constructed by taking the threshold of the selected property so that the subhalo number density matches that of the galaxy sample. Unlike the halo occupation distribution (HOD) method (see Cooray & Sheth 2002, for a review), which is also a frequently used method, SHAM can incorporate subhalo distributions on small scales realized in cosmological N -body simulations.

In performing SHAM, one should use a subhalo property that is expected to strongly correlate with the target galaxy property.

The choice of such a property would have a profound impact on the predicted galaxy statistics, including clustering measurements (e.g., Conroy et al. 2006; Behroozi et al. 2013c; Reddick et al. 2013; Moster et al. 2013; Chaves-Montero et al. 2016; Lehmann et al. 2017; Moster et al. 2018; Behroozi et al. 2019). Thus, comparing the SHAM predictions with observational results can validate the chosen subhalo property. Reddick et al. (2013) used various subhalo properties to study how the predictions for galaxy statistics at $z \simeq 0$ are affected. They showed that using the peak maximum circular velocity of each subhalo in its lifetime, V_{peak} , can reproduce the observed projected correlation functions (PCFs) of the galaxy samples constructed with a threshold of stellar mass and luminosity. Hereafter, we refer to this rank-ordering approach as the V_{peak} model.

However, the validity of using V_{peak} as a proxy for stellar mass or luminosity is still unclear, despite its successful reproduction of observed two-point correlation functions (2PCFs) of some types of galaxies (Nuza et al. 2013; Rodríguez-Torres et al. 2016; Saito et al. 2016; Alam et al. 2017; Dong-Páez et al. 2022). Since satellite subhalos reach V_{peak} before getting accreted onto host halos as shown by Behroozi et al. 2014, the physical relation between V_{peak} and star formation activity in satellite galaxies is uncertain. Campbell et al. (2018) argued that stellar mass growth implied by the V_{peak} model is too early. The implied early growth does not agree with the mass-based SHAM models tuned to match the observed evolution of stellar mass functions (Yang et al. 2012; Behroozi et al. 2013c; Moster et al. 2013). This inconsistency is due to the earlier formation of the gravitational potential well of subhalos than mass (van den Bosch et al. 2014). Interestingly, the rank-ordering model using the

^{*} shogo.masaki@gmail.com

¹ For simplicity, unless explicitly noted, hereafter we shall refer to all halos and subhalos simply as subhalos.

peak mass M_{peak} predicts the growth history similar to the stellar mass function-tuned models. Furthermore, [Leauthaud et al. \(2017\)](#) reported that SHAM and HOD models, including the V_{peak} model ([Reid et al. 2014](#); [Rodríguez-Torres et al. 2016](#); [Saito et al. 2016](#); [Alam et al. 2017](#)), can reproduce the observed PCF of the CMASS galaxies ([Ahn et al. 2014](#)) but overpredict the lensing profile. There are attempts to reconcile the inconsistency between clustering and lensing by incorporating assembly bias ([Wechsler et al. 2006](#); [Gao & White 2007](#)) in the HOD modeling ([Yuan et al. 2020](#)) or re-estimating the lensing measurements ([Lange et al. 2021](#)). However, the situation has not been settled yet. [Hearin et al. \(2013\)](#) also showed that the SHAM models including the V_{peak} model exhibit tensions with the observed luminosity functions of field galaxies and group member galaxies.

[Campbell et al. \(2018\)](#) also studied galaxy clustering predicted by the mass-based SHAM models including the rank-ordering model using the peak mass M_{peak} , and more detailed models for the stellar mass-halo mass relation ([Yang et al. 2012](#); [Behroozi et al. 2013c](#); [Moster et al. 2013](#)). They showed that these models do not reproduce the observed galaxy clustering without introducing assembly bias as the secondary subhalo property ([Masaki et al. 2013b](#); [Hearin & Watson 2013](#)) or invoking the usage of substantial ‘orphans’, i.e., galaxies hosted by subhalos that fall below the numerical resolution limit.

In this paper, we propose a novel rank-ordering mass-based SHAM model. Our model uses the virial mass of the progenitor at a redshift z_{prog} of each subhalo, M_{prog} , as a proxy of the galaxy stellar mass at the time of observation. We refer to this model as the M_{prog} model. We show that our M_{prog} model with a certain choice of z_{prog} can reproduce the observed 2PCFs with the same or higher amplitudes than the V_{peak} model, without the need to invoke orphan galaxies or any secondary subhalo properties. We apply the M_{prog} and V_{peak} models to the latest observed angular correlation functions (ACFs) of the galaxy samples with several stellar mass thresholds at $z \approx 0.4$ obtained from the Subaru Hyper-Suprime Cam (HSC) survey ([Aihara et al. 2018](#); [Ishikawa et al. 2020](#)). For the samples with the thresholds of $9 \leq \log_{10}[M_{*, \text{lim}}/(h^{-2}M_{\odot})] \leq 10.2$, we find that the predictions of the M_{prog} model agree better with the observation than the V_{peak} model at the scales of $< 1 h^{-1} \text{ Mpc}$. We also find that the best-fit z_{prog} , the primary parameter of the M_{prog} model and the characteristic epoch for stellar mass growth, is qualitatively consistent with the two-phase scenario of stellar mass growth in galaxies, i.e., in-situ star formation and ex-situ star accretion ([Oser et al. 2010](#)).

This paper is structured as follows. In Sec. 2, we describe the simulation used in this paper. Then we introduce the M_{prog} model, study how this model predicts the 2PCFs, and discuss how to fit the predictions to the observed ACFs with the stellar mass thresholds. Sec. 3 presents the fitting results on the observed ACFs by both M_{prog} and V_{peak} models, the constrained parameters, the inferred satellite fraction and halo occupation numbers. We summarize our results and conclude in Sec. 4.

2 METHODS

We first present the details of the simulations used in this work, then describe the SHAM model that uses the virial mass of the progenitor at redshift z_{prog} of each subhalo, M_{prog} . We study the 2PCFs predicted by the M_{prog} model and interpret their z_{prog} -dependence. We conclude this section by discussing how we fit the model predictions to observed clustering.

2.1 The mini-Uchuu simulations

We use the publicly available halo/subhalo catalogs produced from the high-resolution mini-Uchuu simulations ([Ishiyama et al. 2021](#)) carried out with the GREEM code ([Ishiyama et al. 2009](#)). The simulation adopts the *Planck* 2018 Λ -cold dark matter (Λ CDM) cosmological parameters as $\Omega_m = 0.3089$, $\Omega_{\Lambda} = 0.6911$, $h = 0.6774$, $\sigma_8 = 0.8159$, $\Omega_b = 0.0486$ and $n_s = 0.9667$, where h is the dimensionless Hubble constant defined by $H_0 = 100h \text{ km s}^{-1} \text{ Mpc}^{-1}$. Other aspects of the simulation are summarized as follows: the number of simulation particles: $N_{\text{part}} = 2560^3$, the simulation box length: $L_{\text{box}} = 400 h^{-1} \text{ Mpc}$, the softening length: $\epsilon = 4.27 h^{-1} \text{ kpc}$, and the mass of a simulation particle: $m_{\text{part}} = 3.27 \times 10^8 h^{-1} M_{\odot}$. The halos and subhalos are identified by the Rockstar finder ([Behroozi et al. 2013a](#)). We utilize the NBODYKIT package ([Hand et al. 2018](#)) to handle the halo/subhalo catalogs.

2.2 Our SHAM model

2.2.1 Motivation

It is known as the downsizing scenario that higher-mass galaxies tend to assemble their stellar mass and cease star formation at earlier epochs, while lower-mass ones tend to continue star formation to later times ([Cowie et al. 1996](#); [Guzmán et al. 1997](#); [Brinchmann & Ellis 2000](#); [Kodama et al. 2004](#); [Bell et al. 2005](#); [Jimenez et al. 2005](#); [Juneau et al. 2005](#); [Bundy et al. 2006](#); [Neistein et al. 2006](#)). In this picture, it is naturally expected that the stellar mass of massive galaxies is better correlated with their progenitors’ host subhalo mass at earlier epochs and vice versa. In other words, we expect that higher-mass galaxies reside in subhalos that were sufficiently massive at higher- z .

The above downsizing-based expectation would be the case for galaxies whose stellar mass growth is dominated by the “in-situ” star formation. For most massive galaxies, we also need to account for stellar mass growth via galaxy mergers, i.e., the “ex-situ” star accretion ([Oser et al. 2010](#); [Lackner et al. 2012](#); [Pillepich et al. 2015](#); [Rodríguez-Gómez et al. 2016](#); [Pillepich et al. 2018b](#); [Davison et al. 2020](#); [Cannarozzo et al. 2022](#)). The process of galaxy mergers increases both the host subhalo and stellar masses. Cosmological simulations of galaxy formation suggest that the fraction of the ex-situ stars in more massive galaxies increases rapidly and can be dominant over or comparable to those formed in-situ at later epochs ([Rodríguez-Gómez et al. 2016](#)). We thus expect that the observed stellar mass of most massive galaxies is represented better by the subhalo mass at epochs nearer the time of observation, instead of some earlier epochs as expected from the downsizing scenarios.

Motivated by these expected correlations between the observed stellar mass and the host subhalo mass, we propose a novel SHAM model. Our model uses the progenitor subhalo mass M_{prog} at an epoch $z = z_{\text{prog}}$ as a proxy of the observed stellar mass, where z_{prog} can vary as a function of the stellar mass.

As we shall see later in Sec. 2.3, the predicted 2PCFs depend on the choice of z_{prog} non-trivially in amplitude and shape. Treating z_{prog} as a free parameter in fitting to observed clustering measurements, the obtained best-fit z_{prog} values should reflect the characteristic epoch of stellar mass growth as a function of the galaxy stellar mass.

As we discussed above, the best-fit z_{prog} values are expected to be lower toward the higher and lower stellar mass ends and have a peak at the intermediate mass range. The lower-mass and higher-mass sides of the peak reflect downsizing in-situ star formation and ex-situ star accretion, respectively.

2.2.2 The implementation

We now describe the implementation of the M_{prog} model. Among the various definitions of the subhalo mass, we use the virial mass given by the ROCKSTAR halo finder as the progenitor mass M_{prog} . We fit the model predictions to observed galaxy clustering with two free parameters. The primary parameter is z_{prog} , the redshift at which we evaluate the virial mass of the progenitor M_{prog} .

The second parameter is to control the scatter between M_* and M_{prog} , σ_M . Although we assume a tight correlation between the two, there could be a non-negligible scatter in the relation. To incorporate such a scatter, we perturb M_{prog} by multiplying the logarithm of M_{prog} with a random number drawn from a Gaussian distribution \mathcal{N} with the mean of 0 and the standard deviation of σ_M (Rodríguez-Torres et al. 2016; Yu et al. 2022) as

$$\log_{10} M_{\text{pert}} = [1 + \mathcal{N}(0, \sigma_M)] \log_{10} M_{\text{prog}}. \quad (1)$$

Such a perturbation leads to more low mass subhalos in the resultant subhalo samples for larger σ_M because they are more abundant than high mass ones. Hence, a larger σ_M suppresses the overall amplitude of 2PCFs.

We construct the mass accretion histories (MAHs; see e.g., Wechsler et al. 2002; McBride et al. 2009) of the most massive progenitors (MMPs) to evaluate M_{prog} using the halo merger trees obtained with the CONSISTENTTREES code (Behroozi et al. 2013b). The MAHs of MMPs can be seen as the main trunk of each merger tree. The available number of the model parameter z_{prog} is limited by the number of outputs of the mini-Uchuu simulations, i.e., 50 outputs from $z = 13.93$ to $z = 0$.

The M_{prog} model is similar to the SHAM model for luminous red galaxies (LRGs) developed by Masaki et al. (2013a). Following observational suggestions on the growth of LRGs, they assumed that the most massive distinct halos at $z = 2$ are the progenitors of LRGs, and identified their descendants at $z \approx 0.3$ as LRGs. They found that their model reproduces observed clustering and lensing profiles qualitatively well. Our M_{prog} model differs in the inclusion of satellite subhalos at z_{prog} and has higher flexibility as z_{prog} is a model parameter.

2.3 The impact of z_{prog} on 2PCFs

We study the impacts of z_{prog} on predicting galaxy clustering. We use the CORRFUNC package (Sinha & Garrison 2019; Sinha & Garrison 2020) to measure the real-space 2PCF ξ as a function of the comoving distance r . For this, we construct subhalo samples at $z = 0$ by taking the threshold M_{prog} value with several z_{prog} so that the number density equals to $n_{\text{gal}} = 10^{-2} h^3 \text{ Mpc}^{-3}$. We estimate the error bars for 2PCFs by the ‘omit-one’ jackknife resampling using the 27 subvolumes. We compare the results with those from the V_{peak} model, which are taken as the fiducial. Below we denote the 2PCFs from the M_{prog} and V_{peak} models as ξ_M and ξ_V , respectively. For simplicity, we do not perturb M_{prog} and V_{peak} .

Fig. 1 shows the impact of z_{prog} on ξ_M at $z = 0$. For ease of comparison, we show ξ_M scaled by ξ_V . The horizontal thin solid line is unity, i.e., ξ_V with the scaled error bars. For understanding the impact of z_{prog} , we show the halo occupation numbers, the average number of galaxies in a halo, $\langle N_{\text{gal}} \rangle$ at $z = 0$ with varying z_{prog} as a function of the virial mass of host central subhalos M_{vir} in Fig. 2. We found a very similar z_{prog} -dependence for two other samples constructed with lower number densities of $n_{\text{gal}} = 10^{-3}$ and $10^{-4} h^3 \text{ Mpc}^{-3}$ at $z = 0$, as well as for the samples with the same three n_{gal} values at $z = 0.5$ and 1.

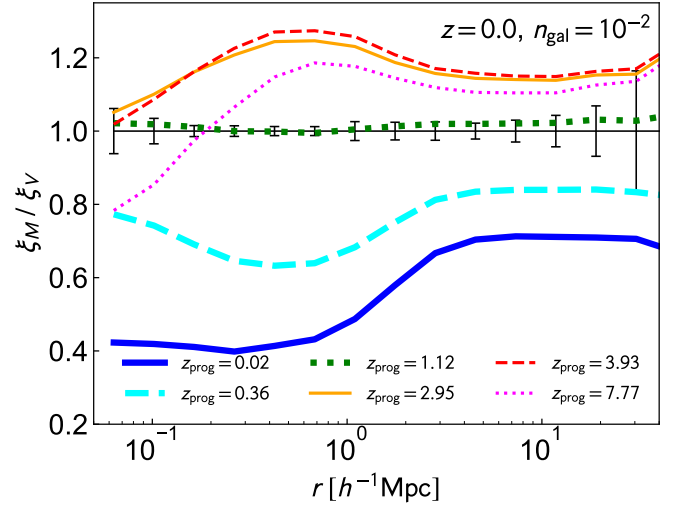


Figure 1. The impact of z_{prog} on ξ_M for the sample with $n_{\text{gal}} = 10^{-2} h^3 \text{ Mpc}^{-3}$ at $z = 0$. ξ_M is scaled by ξ_V . The horizontal thin solid line represents ξ_V with the scaled error bars.

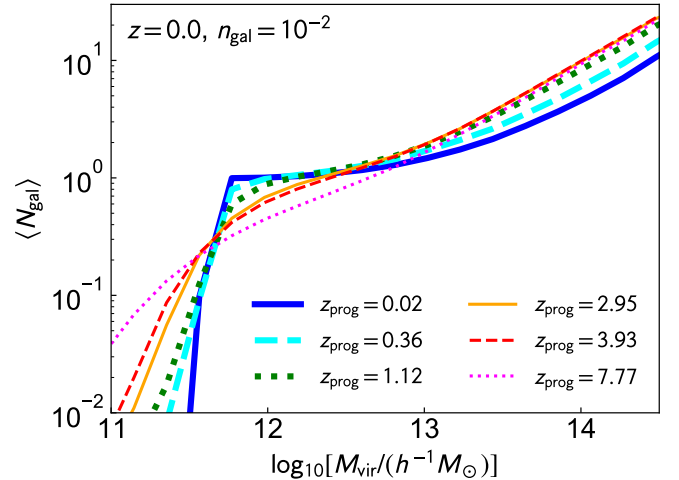


Figure 2. The halo occupation numbers $\langle N_{\text{gal}} \rangle$ of the sample with $n_{\text{gal}} = 10^{-2} h^3 \text{ Mpc}^{-3}$ at $z = 0$ from the M_{prog} model with varying z_{prog} .

It is naively expected that taking a higher- z_{prog} amplifies ξ_M because most massive subhalos at higher- z formed in more biased regions. However, we observe an ‘up-and-down’ trend in the amplitudes of ξ_M for decreasing redshift. That is, it rises from $z_{\text{prog}} \approx 8$ to $z_{\text{prog}} = 3\text{--}4$ and then turns downward to $z_{\text{prog}} \approx 0$. The up trend from $z = 7.77$ to $z \approx 3\text{--}4$ is mainly due to the larger variations in the future MAHs that higher-redshift subhalos will undergo: the descendants of the most massive subhalos at very high- z can be not only well-grown high-mass subhalos but also less-grown low-mass ones at low redshifts. This is clearly seen in Fig. 2 with $\langle N_{\text{gal}} \rangle$ of $z_{\text{prog}} = 7.77$. As a consequence of more low-mass subhalos in the sample, the amplitude of ξ_M is suppressed. This particularly decreases the one-halo term at $r \lesssim 1 h^{-1} \text{ Mpc}$ of ξ_M as Fig. 1 clearly shows the up trend is more prominent at smaller- r . This is because the number of central-satellite pairs in a halo is decreased.

We next discuss the down trend. Fig. 1 shows that the overall amplitude of ξ_M peaks at $z_{\text{prog}} \approx 3\text{--}4$. ξ_M with a lower- z_{prog} is

Table 1. Summary of the incompleteness-corrected number density of each stellar mass threshold sample at $0.30 \leq z < 0.55$ in Ishikawa et al. (2020). The threshold mass is in units of $\log_{10}[M_{*, \text{lim}}/(h^{-2}M_\odot)]$.

threshold mass	$10^3 n_{\text{gal}} [h^3 \text{ Mpc}^{-3}]$
11.0	0.175
10.8	0.596
10.6	1.458
10.4	2.689
10.2	4.838
10.0	7.799
9.8	10.42
9.6	12.68
9.4	16.14
9.2	19.50
9.0	23.36
8.8	27.03
8.6	30.74

more suppressed, especially in the one-halo term range. This is due to the mass stripping of satellite subhalos during accretion onto their host halos (e.g., Reddick et al. 2013). Rank ordering using subhalo mass near the observation time loses satellite subhalos in the resultant sample. This is reflected in Fig. 2 which clearly shows that $\langle N_{\text{gal}} \rangle$ with lower- z_{prog} are more suppressed at the high-mass range due to the loss of satellites. We found that the z_{prog} values at the transition of up and down trend of ξ_M for the sample with $n_{\text{gal}} = 10^{-4} h^3 \text{ Mpc}^{-3}$ is $\simeq 0.6$ and lower than the sample with $n_{\text{gal}} = 10^{-2} h^3 \text{ Mpc}^{-3}$. This is because the satellite fraction of the low- n_{gal} threshold samples is intrinsically low, and then the impact coming from satellite subhalos becomes relatively small. Hence the overall amplitude of ξ_M can keep high for low z_{prog} .

It is known that the V_{peak} model reproduces observed galaxy clustering well. As shown in Fig. 1, the 2PCFs predicted by the M_{prog} model are similar to or even more amplified than those by the V_{peak} model. It is also known that introducing a scatter between the subhalo and the galaxy properties decreases clustering amplitudes. Therefore, by varying z_{prog} and σ_M , the M_{prog} model is expected to reproduce the observed clustering. In Appendix A, we discuss the best matching ξ_M and ξ_V for the subhalo samples constructed with different number density threshold ($n_{\text{gal}} = 10^{-2}, 10^{-3}$ and $10^{-4} h^3 \text{ Mpc}^{-3}$) at $z = 0, 0.5$ and 1 .

2.4 Fitting to observed clustering

In this paper, we fit the predictions of both the M_{prog} and V_{peak} models to the observed ACFs of the photo- z galaxies at $0.30 \leq z < 0.55$ from the Subaru HSC survey measured by Ishikawa et al. (2020). They reported the ACFs for the 13 stellar mass threshold samples with the lower limits from $\log_{10}[M_{*, \text{lim}}/(h^{-2}M_\odot)] = 11$ to 8.6 with a bin size of 0.2 dex. Their observations are attractive because they can measure the ACFs in a stellar mass bin as fine as 0.2 dex and down to a small scale of $\simeq 4 \times 10^{-4}$ deg which corresponds to $\simeq 8 h^{-1} \text{ kpc}$ at $z = 0.43$, using data over a large area of 178 deg^2 of the HSC survey. Table 1 summarizes the number density of each stellar mass threshold sample for which Ishikawa et al. (2020) measured the ACFs. Note that these values are corrected for incompleteness. For the implementation of the two SHAM models, we use the halo/subhalo catalog from the mini-Uchuu simulations at $z = 0.43$, which is close to the peak of the redshift distributions of the observed galaxies.

In fitting the predictions of the M_{prog} model to observed clustering,

as we stated, the two parameters z_{prog} and σ_M are the free parameters. Specifically, we take 40 values for z_{prog} from 0.49 to 13.93, and 20 values for σ_M from 0 to 0.19 with a linear spacing of 0.01. The virial mass at high- z often becomes zero due to the limitation of particle resolution. Large σ_M values include subhalos with $M_{\text{prog}} = 0$ in resultant samples meaning that subhalos are selected randomly in part. Hence, we perturb M_{prog} within only 0.2 dex to avoid this random selection. As discussed in Sec. 2.2.1, we allow for a stellar mass dependence of z_{prog} . As well as z_{prog} , we treat σ_M as a function of the galaxy stellar mass.

We also use the V_{peak} model for comparison. We perturb V_{peak} by the same method as in the M_{prog} model to account for the scatter between V_{peak} and M_* as

$$\log_{10} V_{\text{pert}} = [1 + \mathcal{N}(0, \sigma_V)] \log_{10} V_{\text{peak}}, \quad (2)$$

where σ_V is the standard deviation of the Gaussian distribution \mathcal{N} with the zero-mean. σ_V is the only free parameter and taken to be from 0 to 0.49 with the linear spacing of 0.01. We also treat this parameter as a function of the galaxy stellar mass.

Allowing all free parameters in both models to depend on stellar mass, we construct the subhalo samples corresponding to the stellar mass threshold galaxy samples in a self-consistent manner as follows. First, we assume that the free parameters are constant for the most massive sample, i.e., the sample of $\log_{10}[M_*/(h^{-2}M_\odot)] \geq 11$ in this paper. For this sample, we simply perform the rank-ordering SHAM using the perturbed M_{prog} or V_{peak} . We measure the ACFs for each parameter set and find the best-fit set. Then we temporally exclude the subhalos which are assigned with the sample galaxies by the best-fit parameter set from the whole subhalo catalog. Next, we abundance-match using the rest of the subhalos for the galaxy sample of $10.8 \leq \log_{10}[M_*/(h^{-2}M_\odot)] < 11$ assuming that the free parameters are constant in this narrow range of the stellar mass. The number density of subhalos in this bin given by the difference between the two samples of $\log_{10}[M_*/(h^{-2}M_\odot)] \geq 11$ and $\log_{10}[M_*/(h^{-2}M_\odot)] \geq 10.8$. Combining the subhalos assigned with galaxies of $\log_{10}[M_*/(h^{-2}M_\odot)] \geq 11$ by the best-fit parameter set and the subhalos assigned with galaxies of $10.8 \leq \log_{10}[M_*/(h^{-2}M_\odot)] < 11$ by each parameter set, we obtain the subhalo sample for the galaxies with $\log_{10}[M_*/(h^{-2}M_\odot)] \geq 10.8$. By comparing the predicted ACFs with the observation for the galaxies with $\log_{10}[M_*/(h^{-2}M_\odot)] \geq 10.8$, we obtain the best-fit parameter set for the galaxies of $10.8 \leq \log_{10}[M_*/(h^{-2}M_\odot)] < 11$. We repeat this procedure every 0.2 dex bin until reaching the galaxy sample with $\log_{10}[M_*/(h^{-2}M_\odot)] \geq 8.6$.

To compute the model prediction of ACFs $\omega(\theta)$, we first measure the real-space 2PCFs ξ as a function of the comoving distance r for the subhalo samples constructed with the M_{prog} and V_{peak} models. Then we project ξ along the line of sight to obtain ω using the Limber approximation (Limber 1953; Simon 2007) as

$$\omega(\theta) = 2 \int_0^\infty dz \frac{p^2(z)}{d\chi/dz} \int_0^\infty du \xi \left(r = \sqrt{u^2 + \chi^2(z)\theta^2} \right) \quad (3)$$

$$= 2 \int_0^\infty dz \frac{p^2(z)}{d\chi/dz} \int_{\chi(z)\theta}^\infty dr \frac{r\xi(r)}{\sqrt{r^2 - \chi^2(z)\theta^2}}, \quad (4)$$

where $p(z)$ is the normalized redshift distribution of the observed galaxies², $\chi(z)$ is the comoving distance to the redshift z and u is the comoving distance along the line-of-sight. In doing so, the evolution of ξ over the redshift range $0.30 \leq z < 0.55$ is ignored.

² The observed $p(z)$ in Ishikawa et al. (2020) is kindly provided by S. Ishikawa.

To find the best-fit parameters, we calculate the chi-square values as a function of the parameter set for each threshold sample defined as

$$\chi^2 = \sum_i \frac{(\omega_{\text{obs}, i} - \omega_{\text{model}, i})^2}{\sigma_{\text{obs}, i}^2 + \sigma_{\text{model}, i}^2}, \quad (5)$$

where i denotes the i -th bin of θ , ω_{obs} is the observed ACFs, ω_{model} is the ACFs predicted by the M_{prog} or V_{peak} models, and $\sigma_{\text{obs}, i}$ and $\sigma_{\text{model}, i}$ are the 1σ error for the i -th bin of the observation and the SHAM models, respectively. The 1σ range of the best-fit parameters is given by $\Delta\chi^2 = \chi^2 - \chi^2_{\text{min}}$ where χ^2_{min} is the least chi-square value, $\Delta\chi^2 = 1$ for the V_{peak} model and $\Delta\chi^2 = 2.3$ for the M_{prog} model (Press et al. 1986). We found that the slope of ω_{obs} at $\theta \leq 1 \times 10^{-3}$ deg can be approximated to be $\omega_{\text{obs}} \propto \theta^{-1}$ for almost all samples. This slope is steeper than that at larger angles and thus implies that baryonic effects induce stronger clustering. Hence, for the calculation of the chi-square values, we only use the bins with $\theta > 1 \times 10^{-3}$ deg. Taking $z = 0.43$ as a representative redshift of the observed galaxy sample, the angle corresponds to the comoving distance of $\simeq 20 h^{-1}$ kpc.

3 RESULTS

Here we present the results of fitting to the observed ACFs and show that the M_{prog} model matches with the observations better than the V_{peak} model. We discuss the constrained free parameters in the two models. Finally, we study the inferred satellite fractions and halo occupation numbers.

3.1 The ACFs $\omega(\theta)$ at $z \simeq 0.4$: the observation versus the SHAM models

Fig. 3 compares the observed ACFs and the best-fit predictions from the M_{prog} and V_{peak} models. For clarity, we show $\theta \times \omega(\theta)$ as the vertical axis rather than $\omega(\theta)$. The vertical gray thin lines are the angles corresponding to the comoving distances of 0.1, 1 and $10 h^{-1}$ Mpc at $z = 0.43$. The blue data points with error bars are the observed ACFs measured by Ishikawa et al. (2020). This figure omits the ACFs for the sample with $\log_{10}[M_*/(h^{-2}M_\odot)] \geq 11$ due to the large error bars. The black solid and the red dashed lines with the error bars show the ACFs with the least chi-square values of the M_{prog} and V_{peak} models, respectively. The ACFs given by the parameter sets within the 1σ range are plotted by the light gray and the light pink lines for the M_{prog} and V_{peak} models, respectively.

For the three most massive samples, i.e., the samples with the threshold mass of $\log_{10}[M_{*, \text{lim}}/(h^{-2}M_\odot)] = 10.8, 10.6$ and 10.4 , we see that the best-fit ACFs of both models agree with the observations within the error bars at all scales. This is consistent with the fact that the V_{peak} model works well for clustering of the CMASS galaxies at $z \simeq 0.5$ (Nuza et al. 2013; Rodríguez-Torres et al. 2016; Saito et al. 2016). The situation is different for the samples with $9 \leq \log_{10}[M_{*, \text{lim}}/(h^{-2}M_\odot)] \leq 10.2$. The M_{prog} model predicts ACFs with higher amplitudes than the V_{peak} model over the entire angular range we consider. This is due to the higher satellite fractions of the M_{prog} model (see Sec. 3.3). The best-fit ACFs of both models are consistent with the observations within the error bars at $> 1 h^{-1}$ Mpc. We found that the M_{prog} model agrees with the observations within the error bars at 0.1 – $1 h^{-1}$ Mpc. On the other hand, the V_{peak} model typically underpredicts the observed amplitudes by 20% at the scales of $< 1 h^{-1}$ Mpc. At smaller scales, $< 0.1 h^{-1}$ Mpc, the

Table 2. The best-fit values of parameters for the stellar mass bin samples in the M_{prog} model (σ_M , z_{prog}) and the V_{peak} model (σ_V). The mass range is in units of $\log_{10}[M_*/(h^{-2}M_\odot)]$.

mass range	σ_M	z_{prog}	σ_V
> 11	$0.05^{+0.14}_{-0.05}$	$0.86^{+11.81}_{-0.30}$	$0.17^{+0.00}_{-0.07}$
10.8–11.0	$0.07^{+0.12}_{-0.07}$	$1.12^{+10.38}_{-0.63}$	$0.22^{+0.18}_{-0.03}$
10.6–10.8	$0.06^{+0.13}_{-0.06}$	$2.78^{+7.67}_{-2.18}$	$0.18^{+0.06}_{-0.04}$
10.4–10.6	$0.02^{+0.03}_{-0.02}$	$0.94^{+2.18}_{-0.24}$	$0.11^{+0.04}_{-0.02}$
10.2–10.4	$0.00^{+0.02}_{-0.00}$	$1.65^{+2.62}_{-0.22}$	$0.00^{+0.02}_{-0.00}$
10.0–10.2	$0.00^{+0.01}_{-0.00}$	$4.27^{+0.89}_{-1.65}$	$0.02^{+0.00}_{-0.02}$
9.8–10.0	$0.00^{+0.01}_{-0.00}$	$3.31^{+2.41}_{-0.86}$	$0.00^{+0.02}_{-0.00}$
9.6–9.8	$0.00^{+0.19}_{-0.00}$	$5.15^{+3.43}_{-1.54}$	$0.00^{+0.02}_{-0.00}$
9.4–9.6	$0.00^{+0.01}_{-0.00}$	$3.93^{+2.42}_{-1.31}$	$0.02^{+0.00}_{-0.02}$
9.2–9.4	$0.00^{+0.01}_{-0.00}$	$2.46^{+1.47}_{-0.56}$	$0.00^{+0.02}_{-0.00}$
9.0–9.2	$0.00^{+0.02}_{-0.00}$	$2.03^{+0.43}_{-0.49}$	$0.01^{+0.00}_{-0.01}$
8.8–9.0	$0.00^{+0.03}_{-0.00}$	$1.22^{+0.32}_{-0.19}$	$0.00^{+0.01}_{-0.00}$
8.6–8.8	$0.00^{+0.19}_{-0.00}$	$0.94^{+0.18}_{-0.39}$	$0.20^{+0.29}_{-0.08}$

M_{prog} model still works better than the V_{peak} model but underpredicts the observation typically by 15%. This implies that the M_{prog} model needs fine-tuning for more accurate modeling of galaxy-subhalo connections. It is unlikely due to the lack of resolution of the mini-Uchuu simulations because the ACFs of the two lowest mass samples, i.e., the samples with the lower limits of $\log_{10}[M_{*, \text{lim}}/(h^{-2}M_\odot)] = 8.8$ and 8.6 , are reproduced well by both models.

3.2 The constrained parameters

The best-fit parameters σ_M , z_{prog} in the M_{prog} model and σ_V in the V_{peak} model for the stellar mass bin samples are summarized in Table 2 and plotted in Figs. 4 and 5 as functions of the stellar mass range.

The parameters of the M_{prog} model, z_{prog} and σ_M , are poorly constrained in our considered range for the three highest mass ranges, i.e., > 11 , 10.8 – 11 and 10.6 – 10.8 in units of $\log_{10}[M_*/(h^{-2}M_\odot)]$. The large error bars of $\omega(\theta)$ prevent us from breaking the degeneracy between the two parameters.

The scatter parameters, σ_M and σ_V , are constrained weakly for the lowest mass range, $8.6 \leq \log_{10}[M_*/(h^{-2}M_\odot)] < 8.8$, despite the high precision of the observed ACF. This is because the galaxies in the mass range are assigned in the lowest mass and the most abundant subhalos, and perturbing the stellar mass proxy is less effective in predicting galaxy clustering. For the other intermediate-mass ranges, the scatter parameters are close to zero. This is simply because the ACFs predicted by the M_{prog} and V_{peak} models lack amplitude compared to the observations at small scales. The only exception is the mass range of $9.6 \leq \log_{10}[M_*/(h^{-2}M_\odot)] < 9.8$. The large error bar of σ_M for this range is caused by the ‘up-and-down’ dependence of clustering on z_{prog} (see Sec. 2.3). The best fit z_{prog} for this mass range is at the peak of the up-and-down trend of clustering. Hence the ACFs with similar amplitude and shape can be given by the parameter sets of z_{prog} around the best-fit values and the varying σ_M values.

The constrained characteristic redshift of the M_{prog} model, z_{prog} , displays an interesting feature. As shown in the lower panel of Fig. 4, z_{prog} as a function of the stellar mass range appears to peak at $9.6 \leq \log_{10}[M_*/(h^{-2}M_\odot)] < 9.8$. As discussed in Sec. 2.2.1, this feature is expected and related to the two phases of stellar mass growth in galaxies. In the two-phase formation scenario, the best-fit z_{prog} would increase toward the high mass range of the in-situ star-

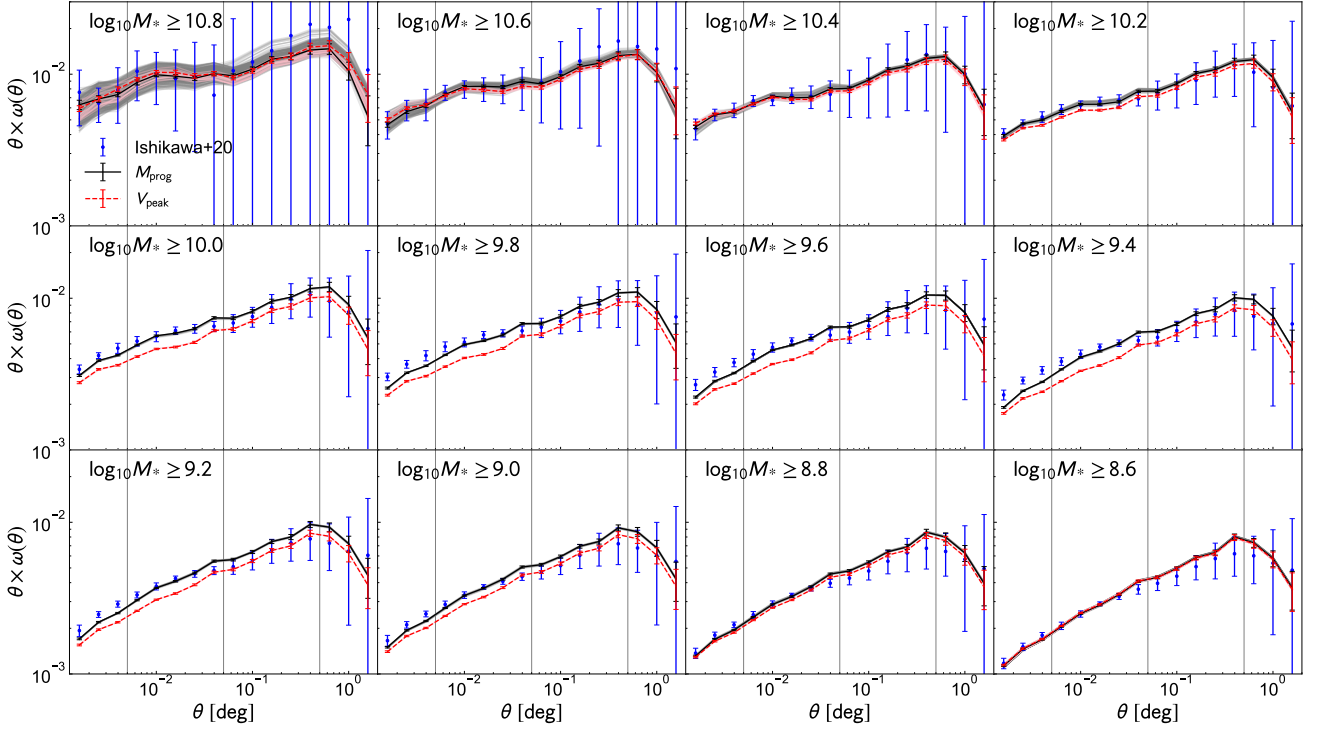


Figure 3. The ACFs $\omega(\theta)$ at $z \approx 0.4$ of the stellar mass threshold samples. The mass ranges are noted in each panel, where the stellar mass M_* is in units of $h^{-2} M_\odot$. The blue data points with error bars are the observational results (Ishikawa et al. 2020). The black solid and the red dashed lines show the predictions by the M_{prog} and V_{peak} models, respectively. The vertical gray solid lines are the angles corresponding to comoving scales of 0.1, 1, and $10 h^{-1} \text{ Mpc}$ at $z = 0.43$, respectively.

forming galaxies and decrease toward massive end galaxies in which the ex-situ star accretion is effective. In other words, the best-fit z_{prog} as a function of the galaxy stellar mass has a peak at the intermediate mass. This is indeed seen in the lower panel of Fig. 4. Also, it is suggested that the ex-situ star accretion is efficient for the galaxies with $\log_{10}[M_*/(h^{-2} M_\odot)] \gtrsim 9.8$ at $z = 0.4$, and the in-situ star formation is dominant in the lower mass galaxies.

3.3 The inferred satellite fraction

Fig. 6 shows the satellite fraction f_{sat} for the threshold samples as a function of the threshold mass $\log_{10}[M_{*, \text{lim}}/(h^{-2} M_\odot)]$ inferred by the M_{prog} and V_{peak} models. For each threshold sample with the best-fit parameter set, f_{sat} is simply measured as

$$f_{\text{sat}} = \frac{\text{number of galaxies hosted by satellite subhalos}}{\text{total number of galaxies}}. \quad (6)$$

The error bars are the range given by the parameter sets within the 1σ error.

The overall shape of the satellite fraction differs between the M_{prog} and V_{peak} models. The V_{peak} model yields a monotonically decreasing form with increasing stellar mass. One would naively expect that the satellite fraction to be higher for lower mass galaxies, as the V_{peak} model predicts. However, in the M_{prog} model, f_{sat} as a function of the lower stellar mass limit has a single peak at $\log_{10}[M_{*, \text{lim}}/(h^{-2} M_\odot)] \approx 9.3$.

The amplitude of galaxy clustering is strongly related to the satellite fraction. For the threshold samples with $\log_{10}[M_{*, \text{lim}}/(h^{-2} M_\odot)] \geq 10.4$ and $\log_{10}[M_{*, \text{lim}}/(h^{-2} M_\odot)] = 8.6$, the ACFs of the M_{prog} and V_{peak} models are consistent with

each other (and the observations). The two models predict the satellite fractions very close to each other for these samples. For the other threshold samples with $8.8 \leq \log_{10}[M_{*, \text{lim}}/(h^{-2} M_\odot)] \leq 10.2$, the M_{prog} model gives the higher f_{sat} than the V_{peak} model as well as the amplitudes of the ACFs. This implies the higher amplitude of the correlation functions predicted by the M_{prog} model is due to the higher satellite fraction.

Fig. 7 is very similar to Fig. 6 but shows the inferred satellite fraction f_{sat} for the stellar mass bin samples as a function of the mass range. Compared to f_{sat} for the threshold samples, the peak of the M_{prog} model is shifted to a higher stellar mass, $\log_{10}[M_*/(h^{-2} M_\odot)] \approx 9.7$, because f_{sat} for the threshold samples is the cumulation of f_{sat} for the bin samples.

Knobel et al. (2013) used the spectroscopic galaxy sample at $0.1 < z < 0.8$ from the zCOSMOS survey to evaluate the satellite fractions (see van den Bosch et al. 2008, for the measurements at $z \approx 0$). They showed that the satellite fractions at $0.4 < z < 0.6$ and $0.6 < z < 0.8$ are not a monotonic function of the stellar mass, and have a peak at $\log_{10}[M_*/(h^{-2} M_\odot)] \approx 10.1$ and 10.3 , respectively. This is similar to the prediction of the M_{prog} model.

The stellar mass dependence of the satellite fraction of the M_{prog} model comes from the best-fit z_{prog} . The peak positions and shapes of the satellite fraction and the best-fit z_{prog} (the lower panel of Fig. 4) are very similar to each other. This is because a larger z_{prog} generally leads to a higher satellite fraction as discussed in Sec. 2.3.

3.4 The inferred halo occupation numbers

Fig. 8 shows the inferred halo occupation numbers of the subhalo samples given by the best-fit parameter sets for each threshold sample

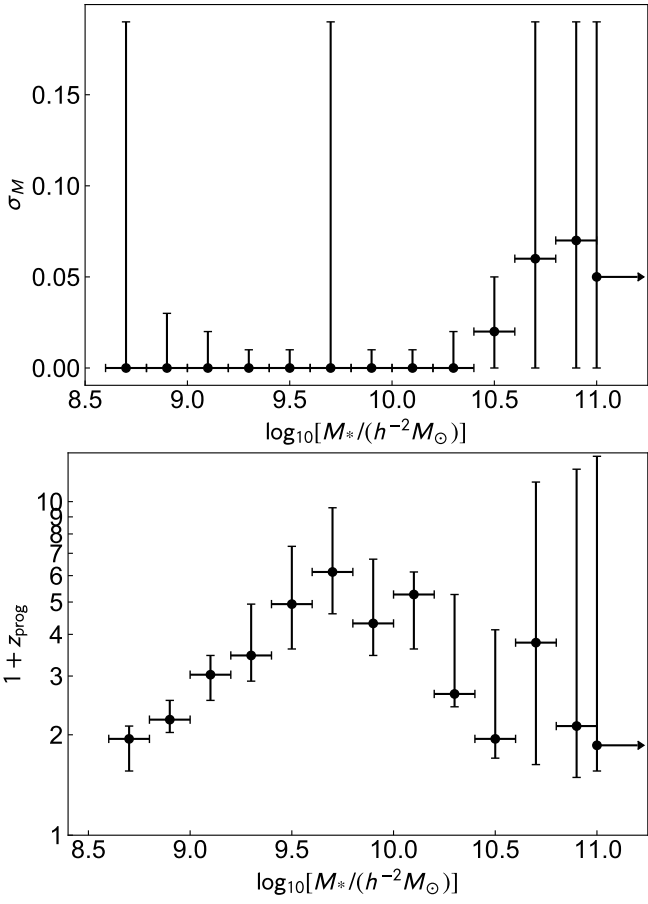


Figure 4. The best-fit parameters of the M_{prog} model, σ_M (upper panel) and z_{prog} (lower panel) for the stellar mass bin samples. The error bars represent 1σ uncertainty. Note that only the highest mass range represents the threshold sample of $\log_{10}[M_*/(h^{-2}M_\odot)] \geq 11$, not a binned one.

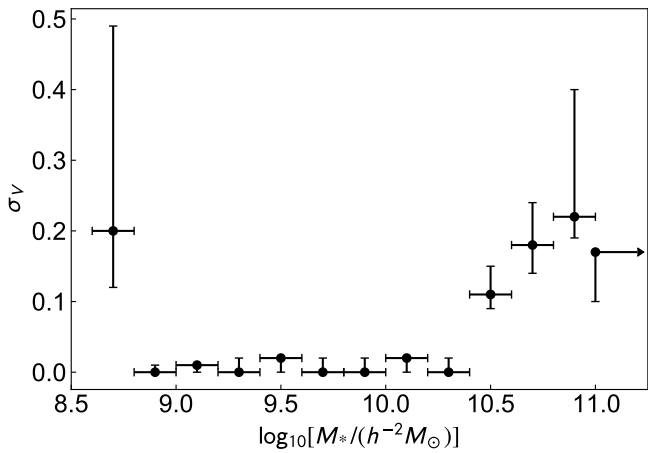


Figure 5. Similar to Fig. 4 but for the best-fit parameter in the V_{peak} model, σ_V .

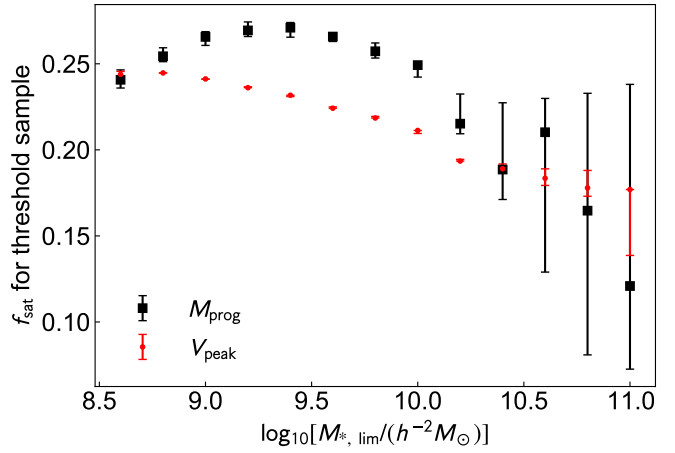


Figure 6. The satellite fraction f_{sat} of the threshold sample as a function of the threshold mass $\log_{10}[M_{*, \text{lim}}/(h^{-2}M_\odot)]$ inferred by the M_{prog} model (the black square points) and the V_{peak} model (the red small dot points).

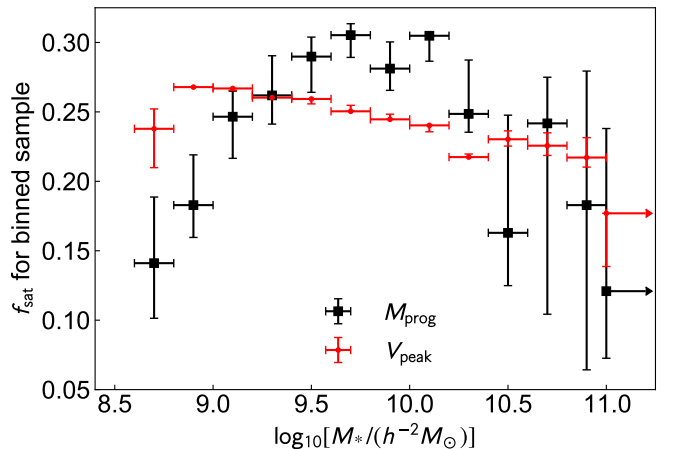


Figure 7. Very similar to Fig. 6 but the inferred satellite fractions for the stellar mass bin samples.

as the solid lines. The dashed and dotted lines represent the halo occupation numbers of central and satellite galaxies, respectively. The thick black and thin red lines are the results with the best-fit parameter sets of the M_{prog} and V_{peak} models, respectively. The halo occupation numbers given by the parameter sets within the 1σ range are represented by the light gray (the M_{prog} model) and pink (the V_{peak} model) lines.

For the three highest and the two lowest mass samples for which both models give the ACFs consistent with the observation, the halo occupation numbers of the M_{prog} and V_{peak} models are consistent with each other within the 1σ error. For the other mass threshold samples with $9 \leq \log_{10}[M_*/(h^{-2}M_\odot)] \leq 10.2$, the M_{prog} model preferentially assigns both central and satellite galaxies in lower mass subhalos than the V_{peak} model. It should be noted that the M_{prog} model predicts ACFs with higher amplitudes than the V_{peak} model even in the two-halo term regime, i.e., $>$ a few h^{-1} Mpc, as shown in Fig. 3. This implies that the M_{prog} model preferentially selects highly biased (or early-forming) low-mass subhalos.

We also study the halo occupation numbers for the stellar mass bin samples in Fig. 9. The biggest difference from the halo occupation

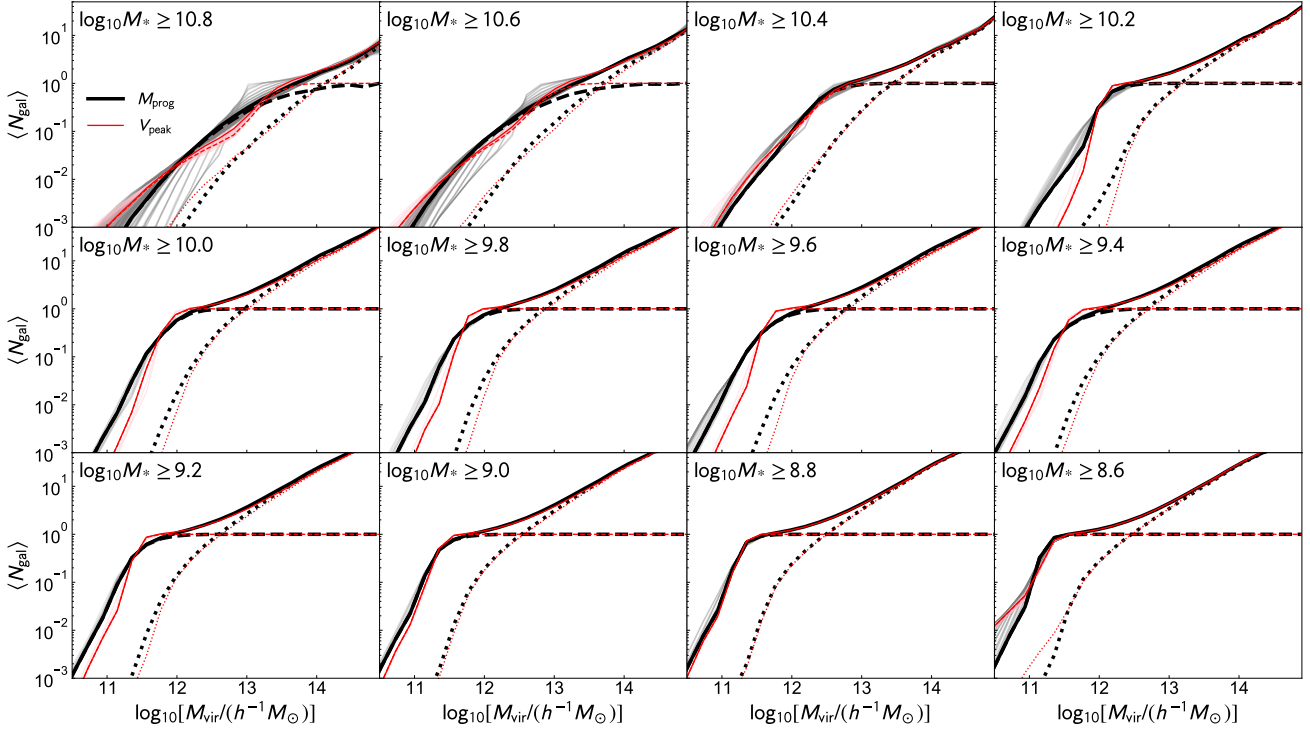


Figure 8. The solid lines show the inferred halo occupation numbers $\langle N_{\text{gal}} \rangle$ as a function of the virial mass of the host central subhalo M_{vir} for each threshold sample. The mass ranges are noted in each panel, where the stellar mass M_* is in units of $h^{-2} M_{\odot}$. The dashed and dotted lines represent the halo occupation numbers of central and satellite galaxies, respectively. The thick black and thin red lines are the results with the best-fit parameter sets of the M_{prog} and V_{peak} models, respectively. The halo occupation numbers given by the parameter sets within the 1σ range are represented by the light gray (the M_{prog} model) and pink (the V_{peak} model) lines.

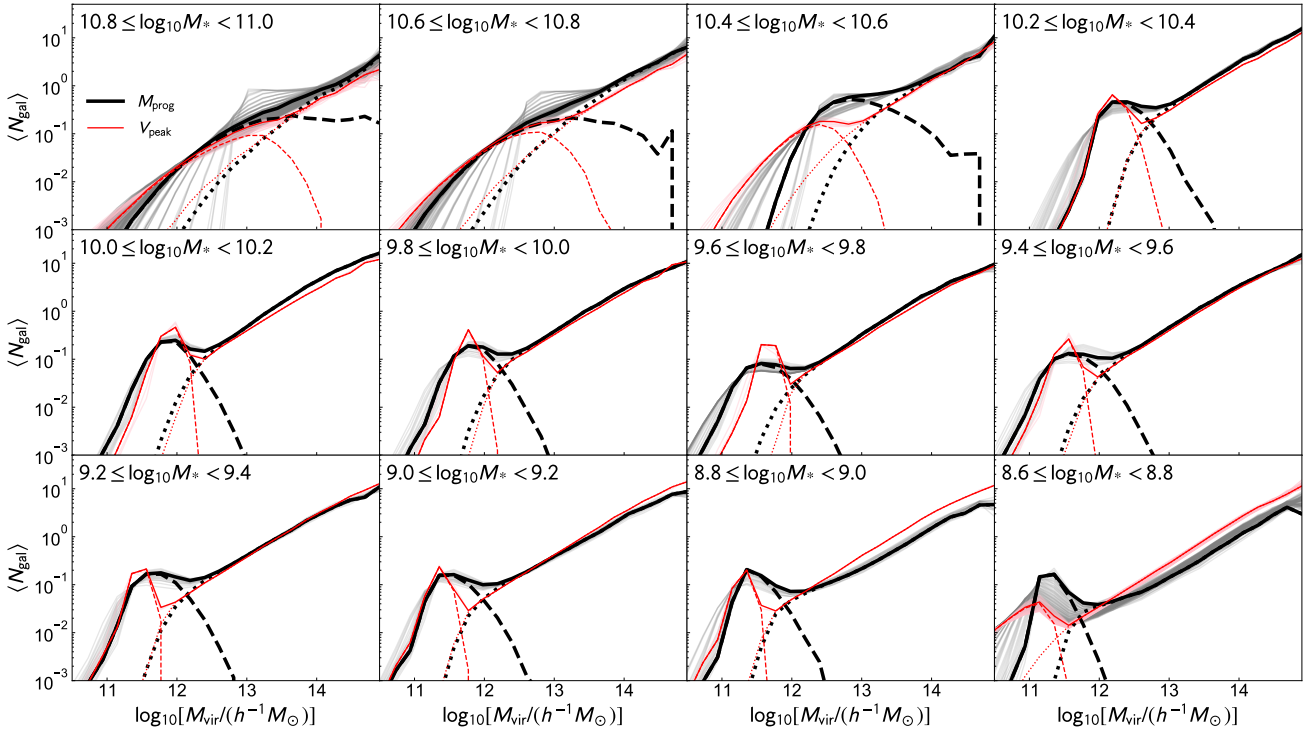


Figure 9. Same as Fig. 8 but the halo occupation numbers inferred for the stellar mass bin samples.

numbers for the threshold samples is that the M_{prog} model assigns the central galaxies in higher mass halos for all mass bins. This means that there are more central-satellite galaxy pairs in the M_{prog} model than in the V_{peak} model. Hence, together with the higher satellite fractions, the M_{prog} model predicts an enhanced galaxy clustering signal at the smallest scales than the V_{peak} model. It also can be said that using observed clustering of stellar mass bin samples is more useful to examine SHAM models because the differences between the two models are larger than the halo occupation numbers for the threshold samples.

4 SUMMARY AND CONCLUSION

We have proposed a novel rank-ordering SHAM model using the progenitor virial mass of each subhalo at redshift z_{prog} , M_{prog} , as a proxy of galaxy stellar mass at the time of observation. In this model, the characteristic redshift z_{prog} at which we evaluate M_{prog} , and the scatter parameter σ_M (see Eq. 1) are the free fitting parameters. The motivation of this model is related to the two-phase scenario of stellar mass growth in galaxies, i.e., in-situ star formation and ex-situ star accretion (see Sec. 2.2.1).

We have studied the z_{prog} -dependence of the 2PCFs ξ for the subhalo samples with the number density of $n_{\text{gal}} = 10^{-2} h^3 \text{ Mpc}^{-3}$ at $z = 0$ (Fig. 1). The z_{prog} -dependence can be understood by the variation of subhalo mass accretion histories and the subhalo mass stripping during accretion as shown in the halo occupation number (Fig. 2). We have shown that the M_{prog} model with certain z_{prog} value gives the 2PCFs similar to or even more amplified than those by the V_{peak} model. We expect the M_{prog} model to be able to well reproduce the observed galaxy clustering signal.

We have applied the M_{prog} and V_{peak} models to the observed ACFs ω of the photo- z selected galaxies at $z \simeq 0.4$ from the Subaru HSC survey (Ishikawa et al. 2020). Both models can reproduce the observed ACFs for the stellar mass threshold samples with $\log_{10}[M_{*,\text{lim}}/(h^{-2} M_{\odot})] \geq 10.4$ and $\log_{10}[M_{*,\text{lim}}/(h^{-2} M_{\odot})] \leq 8.8$ (Fig. 3). We have also shown that the V_{peak} model under-predicts the amplitude of ACFs at the scale of $< 1 h^{-1} \text{ Mpc}$ and fails to match the observed ACFs for the samples of $9 \leq \log_{10}[M_{*,\text{lim}}/(h^{-2} M_{\odot})] \leq 10.2$. On the other hand, the M_{prog} model gives sufficiently higher amplitudes and agrees with the observations within the error bars at $0.1-1 h^{-1} \text{ Mpc}$ for these samples.

We have found that z_{prog} constrained by the observed ACFs has an interesting dependence on the stellar mass (the lower panel of Fig. 4). The best-fit z_{prog} is lower toward the lowest and highest stellar mass ranges and has a single peak at $\log_{10}[M_{\text{*/}}/(h^{-2} M_{\odot})] \simeq 9.7$. This trend is qualitatively consistent with the in-/ex-situ scenario of stellar mass growth. It is clearly important to quantitatively examine whether the obtained values of z_{prog} are physically reasonable. Specifically, investigating what events related to stellar mass growth happened at $z = z_{\text{prog}}$ should be an interesting topic. The recent cosmological simulations of galaxy formation (e.g., EAGLE; Crain et al. 2015; Schaye et al. 2015; Illustris TNG; Weinberger et al. 2017; Pillepich et al. 2018a; FIREbox; Feldmann et al. 2022) might give clues to understanding the physical origin of the constrained z_{prog} values, although it is beyond the scope of this work.

We have studied the inferred satellite fractions in Figs. 6 & 7. The successful agreement of the M_{prog} model with the observed ACFs for the samples with the thresholds of $9 \leq \log_{10}[M_{*,\text{lim}}/(h^{-2} M_{\odot})] \leq 10.2$ is attributed to the higher satellite fraction than in the V_{peak} model. For the other mass-threshold samples for which both models can reproduce the observed ACFs, the predicted satellite fractions

from the two models agree with each other. Thus the satellite fraction is a crucial factor for determining the strength of galaxy clustering.

We have found notable differences in the inferred halo occupation numbers between the M_{prog} and V_{peak} models (Figs. 8 & 9). For the three highest and the two lowest mass samples for which both models match the observed ACFs, the halo occupation numbers are consistent with each other within the 1σ error of the fitted parameters. For the samples with $9 \leq \log_{10}[M_{*,\text{lim}}/(h^{-2} M_{\odot})] \leq 10.2$, the M_{prog} model predicts more amplified ACFs and is more successful in reproducing the observations by populating galaxies with lower mass subhalos.

In future work, we plan to examine the M_{prog} SHAM model by comparing it with observed galaxy statistics as a function of the stellar mass including clustering measurements at various redshifts (e.g., Yang et al. 2012; Ishikawa et al. 2020; Shuntov et al. 2022), the satellite fractions as a function of the stellar mass (van den Bosch et al. 2008; Knobel et al. 2013), the mass profiles around galaxies (Mandelbaum et al. 2006; Leauthaud et al. 2012) and the group statistics (Hearin et al. 2013). Especially, it is interesting to apply to the “lensing is low” problem on the CMASS galaxies. Leauthaud et al. (2017) showed that SHAM and HOD models, including the V_{peak} model, can reproduce the observed PCF of the CMASS galaxies but overpredict the lensing profile. Since, as we stated, galaxies tend to live in lower mass halos in the M_{prog} model than the V_{peak} model while keeping the clustering amplitudes, the M_{prog} model may be able to match better the observed CMASS clustering and lensing simultaneously.

With only one more free parameter than the V_{peak} model, the M_{prog} model is shown to be highly flexible and can more faithfully reproduce the observed ACFs, providing a more physical way to interpret the observed clustering measurements. The findings in this paper would be an important step toward accurate modeling of the galaxy-halo connection.

ACKNOWLEDGEMENTS

We would like to thank Yoshiaki Matsuoka for useful discussions in the early stage of this work, Tomoaki Ishiyama for the details of the Uchuu simulations, Shogo Ishikawa for sharing his data with us, and Peter Behroozi and Masato Shirasaki for useful comments on the manuscript. The calculations in part were carried out on Cray XC50 at Center for Computational Astrophysics, National Astronomical Observatory of Japan. This work was supported in part by JSPS KAKENHI Grant Numbers JP19H00677, JP21H05465, JP22K03644 (SM), and JP21K13956 (DK). YTL acknowledges support from the National Science and Technology Council of Taiwan under grants MOST 111-2112-M-001-043 and MOST 110-2112-M-001-004.

DATA AVAILABILITY

The Uchuu simulations are available at <http://skiesanduniverses.org/Simulations/Uchuu/>. Other data presented in this paper can be provided by the authors upon request.

REFERENCES

- Ahn C. P., et al., 2014, *ApJS*, 211, 17
- Aihara H., et al., 2018, *PASJ*, 70, S4
- Alam S., Miyatake H., More S., Ho S., Mandelbaum R., 2017, *MNRAS*, 465, 4853

Behroozi P. S., Wechsler R. H., Wu H.-Y., 2013a, *ApJ*, **762**, 109
 Behroozi P. S., Wechsler R. H., Wu H.-Y., Busha M. T., Klypin A. A., Primack J. R., 2013b, *ApJ*, **763**, 18
 Behroozi P. S., Wechsler R. H., Conroy C., 2013c, *ApJ*, **770**, 57
 Behroozi P. S., Wechsler R. H., Lu Y., Hahn O., Busha M. T., Klypin A., Primack J. R., 2014, *ApJ*, **787**, 156
 Behroozi P., Wechsler R. H., Hearin A. P., Conroy C., 2019, *MNRAS*, **488**, 3143
 Bell E. F., et al., 2005, *ApJ*, **625**, 23
 Brinchmann J., Ellis R. S., 2000, *ApJ*, **536**, L77
 Bundy K., et al., 2006, *ApJ*, **651**, 120
 Campbell D., van den Bosch F. C., Padmanabhan N., Mao Y.-Y., Zentner A. R., Lange J. U., Jiang F., Villarreal A. S., 2018, *MNRAS*, **477**, 359
 Cannarozzo C., et al., 2022, arXiv e-prints, p. [arXiv:2210.08109](https://arxiv.org/abs/2210.08109)
 Chaves-Montero J., Angulo R. E., Schaye J., Schaller M., Crain R. A., Furlong M., Theuns T., 2016, *MNRAS*, **460**, 3100
 Conroy C., Wechsler R. H., Kravtsov A. V., 2006, *ApJ*, **647**, 201
 Cooray A., Sheth R., 2002, *Phys. Rep.*, **372**, 1
 Cowie L. L., Songaila A., Hu E. M., Cohen J. G., 1996, *AJ*, **112**, 839
 Crain R. A., et al., 2015, *MNRAS*, **450**, 1937
 Davison T. A., Norris M. A., Pfeffer J. L., Davies J. J., Crain R. A., 2020, *MNRAS*, **497**, 81
 Dong-Páez C. A., et al., 2022, arXiv e-prints, p. [arXiv:2208.00540](https://arxiv.org/abs/2208.00540)
 Feldmann R., et al., 2022, arXiv e-prints, p. [arXiv:2205.15325](https://arxiv.org/abs/2205.15325)
 Gao L., White S. D. M., 2007, *MNRAS*, **377**, L5
 Guzmán R., Gallego J., Koo D. C., Phillips A. C., Lowenthal J. D., Faber S. M., Illingworth G. D., Vogt N. P., 1997, *ApJ*, **489**, 559
 Hand N., Feng Y., Beutler F., Li Y., Modi C., Seljak U., Slepian Z., 2018, *AJ*, **156**, 160
 Hearin A. P., Watson D. F., 2013, *MNRAS*, **435**, 1313
 Hearin A. P., Zentner A. R., Berlind A. A., Newman J. A., 2013, *MNRAS*, **433**, 659
 Ishikawa S., et al., 2020, *ApJ*, **904**, 128
 Ishiyama T., Fukushige T., Makino J., 2009, *PASJ*, **61**, 1319
 Ishiyama T., et al., 2021, *MNRAS*, **506**, 4210
 Jimenez R., Panter B., Heavens A. F., Verde L., 2005, *MNRAS*, **356**, 495
 Juneau S., et al., 2005, *ApJ*, **619**, L135
 Knobel C., et al., 2013, *ApJ*, **769**, 24
 Kodama T., et al., 2004, *MNRAS*, **350**, 1005
 Kravtsov A. V., Berlind A. A., Wechsler R. H., Klypin A. A., Gottlöber S., Allgood B., Primack J. R., 2004, *ApJ*, **609**, 35
 Lackner C. N., Cen R., Ostriker J. P., Joung M. R., 2012, *MNRAS*, **425**, 641
 Lange J. U., Leauthaud A., Singh S., Guo H., Zhou R., Smith T. L., Cyr-Racine F.-Y., 2021, *MNRAS*, **502**, 2074
 Leauthaud A., et al., 2012, *ApJ*, **744**, 159
 Leauthaud A., et al., 2017, *MNRAS*, **467**, 3024
 Lehmann B. V., Mao Y.-Y., Becker M. R., Skillman S. W., Wechsler R. H., 2017, *ApJ*, **834**, 37
 Limber D. N., 1953, *ApJ*, **117**, 134
 Mandelbaum R., Seljak U., Kauffmann G., Hirata C. M., Brinkmann J., 2006, *MNRAS*, **368**, 715
 Masaki S., Hikage C., Takada M., Spergel D. N., Sugiyama N., 2013a, *MNRAS*, **433**, 3506
 Masaki S., Lin Y.-T., Yoshida N., 2013b, *MNRAS*, **436**, 2286
 McBride J., Fakhouri O., Ma C.-P., 2009, *MNRAS*, **398**, 1858
 Moster B. P., Naab T., White S. D. M., 2013, *MNRAS*, **428**, 3121
 Moster B. P., Naab T., White S. D. M., 2018, *MNRAS*, **477**, 1822
 Neistein E., van den Bosch F. C., Dekel A., 2006, *MNRAS*, **372**, 933
 Nuza S. E., et al., 2013, *MNRAS*, **432**, 743
 Oser L., Ostriker J. P., Naab T., Johansson P. H., Burkert A., 2010, *ApJ*, **725**, 2312
 Pillepich A., Madau P., Mayer L., 2015, *ApJ*, **799**, 184
 Pillepich A., et al., 2018a, *MNRAS*, **473**, 4077
 Pillepich A., et al., 2018b, *MNRAS*, **475**, 648
 Press W. H., Flannery B. P., Teukolsky S. A., 1986, Numerical recipes. The art of scientific computing
 Reddick R. M., Wechsler R. H., Tinker J. L., Behroozi P. S., 2013, *ApJ*, **771**, 30

Table A1. Summary of the z_{prog} values in the M_{prog} model which gives the best matched-2PCFs to the V_{peak} model, and $\langle z_{\text{peak}} \rangle$ for the V_{peak} model at $z = 0$, 0.5 and 1 for the three samples.

	$n_{\text{gal}} [h^3 \text{ Mpc}^{-3}]$	$z = 0$	$z = 0.5$	$z = 1$
z_{prog}	10^{-2}	1.12	1.43	1.77
	10^{-3}	0.63	1.03	1.54
	10^{-4}	0.36	0.86	1.43
$\langle z_{\text{peak}} \rangle$	10^{-2}	1.07	1.35	1.75
	10^{-3}	0.68	1.04	1.50
	10^{-4}	0.45	0.86	1.35

Reid B. A., Seo H.-J., Leauthaud A., Tinker J. L., White M., 2014, *MNRAS*, **444**, 476
 Rodriguez-Gomez V., et al., 2016, *MNRAS*, **458**, 2371
 Rodríguez-Torres S. A., et al., 2016, *MNRAS*, **460**, 1173
 Saito S., et al., 2016, *MNRAS*, **460**, 1457
 Schaye J., et al., 2015, *MNRAS*, **446**, 521
 Shuntov M., et al., 2022, *A&A*, **664**, A61
 Simon P., 2007, *A&A*, **473**, 711
 Sinha M., Garrison L., 2019, in Majumdar A., Arora R., eds, Software Challenges to Exascale Computing. Springer Singapore, Singapore, pp 3–20, https://doi.org/10.1007/978-981-13-7729-7_1
 Sinha M., Garrison L. H., 2020, *MNRAS*, **491**, 3022
 Wechsler R. H., Tinker J. L., 2018, *ARA&A*, **56**, 435
 Wechsler R. H., Bullock J. S., Primack J. R., Kravtsov A. V., Dekel A., 2002, *ApJ*, **568**, 52
 Wechsler R. H., Zentner A. R., Bullock J. S., Kravtsov A. V., Allgood B., 2006, *ApJ*, **652**, 71
 Weinberger R., et al., 2017, *MNRAS*, **465**, 3291
 Yang X., Mo H. J., van den Bosch F. C., Zhang Y., Han J., 2012, *ApJ*, **752**, 41
 Yu J., et al., 2022, *MNRAS*, **516**, 57
 Yuan S., Eisenstein D. J., Leauthaud A., 2020, *MNRAS*, **493**, 5551
 van den Bosch F. C., Aquino D., Yang X., Mo H. J., Pasquali A., McIntosh D. H., Weinmann S. M., Kang X., 2008, *MNRAS*, **387**, 79
 van den Bosch F. C., Jiang F., Hearin A., Campbell D., Watson D., Padmanabhan N., 2014, *MNRAS*, **445**, 1713

APPENDIX A: COMPARISONS BETWEEN THE M_{prog} AND V_{peak} MODELS

We here compare the 2PCFs given by the M_{prog} and V_{peak} models denoted as ξ_M and ξ_V , respectively. As in Sec. 2.3, we measure ξ_M and ξ_V for the subhalo samples with the number densities of $n_{\text{gal}} = 10^{-2}$, 10^{-3} and $10^{-4} h^3 \text{ Mpc}^{-3}$ at $z = 0$, 0.5 and 1. We seek z_{prog} that gives the best matched- ξ_M to ξ_V . For simplicity, we do not perturb either M_{prog} or V_{peak} .

We find that ξ_M with a certain z_{prog} value matches with ξ_V very well for all three samples at all three redshifts. Table A1 summarizes the best match z_{prog} values for each sample at $z = 0$, 0.5 and 1. Fig. A1 compares ξ_M with the best match z_{prog} and ξ_V for the three samples at $z = 0$, 0.5 and 1, and shows a fairly good agreement between them.

This nice agreement is understood by the mean redshift at which V_{peak} is achieved, $\langle z_{\text{peak}} \rangle$. Table A1 also summarizes the $\langle z_{\text{peak}} \rangle$ values for the samples at the redshifts. We find that the best match z_{prog} and $\langle z_{\text{peak}} \rangle$ are very close to each other within a difference of less than $z = 0.1$. Hence the V_{peak} model is equivalent to selecting most massive subhalos at a somewhat higher redshift. We also compute the matching rate between the subhalo samples from the M_{prog} model with the best match z_{prog} and ones from the V_{peak} model. The

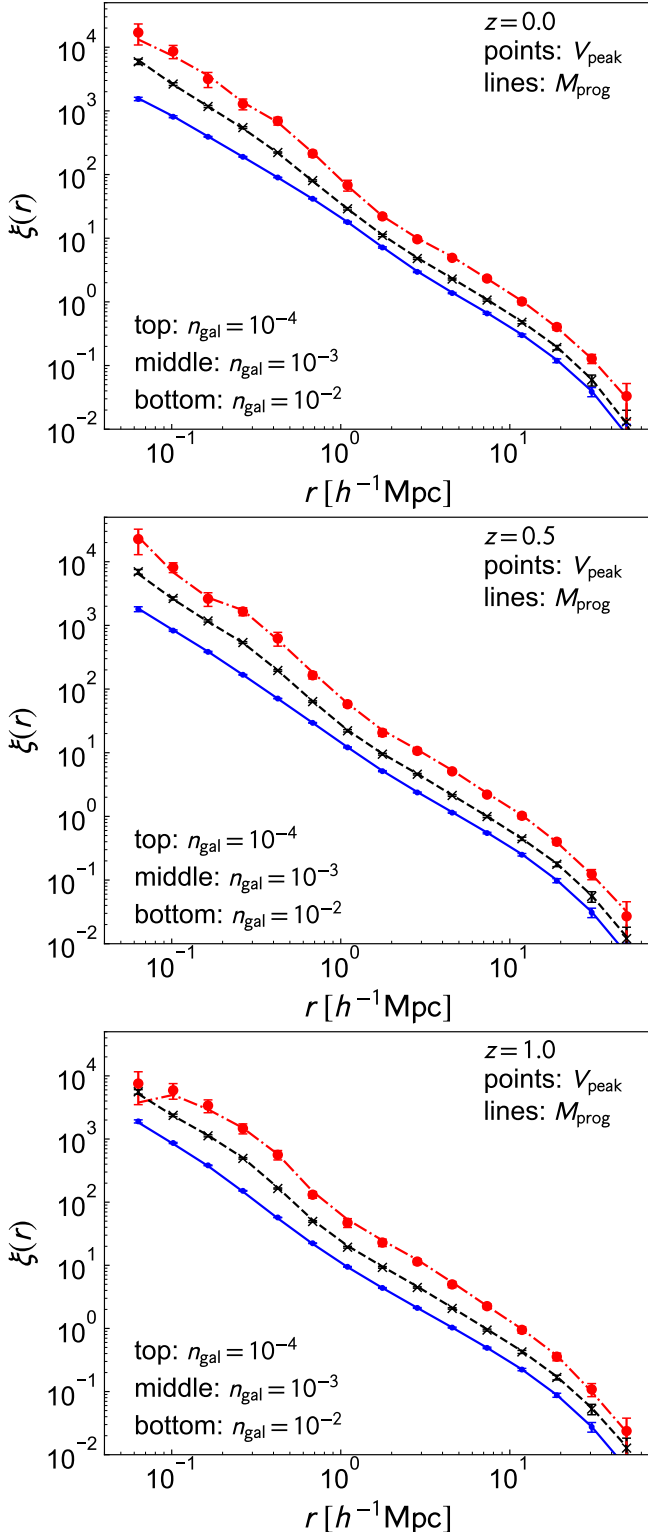


Figure A1. Comparisons between ξ_M and ξ_V for the three samples at $z = 0, 0.5$ and 1 . For the M_{prog} model, the best match z_{prog} is adopted for each sample.

Table A2. Summary of the matching rates between the subhalo samples from the M_{prog} model with the best match z_{prog} for each sample and from the V_{peak} model at $z = 0, 0.5$ and 1 .

$n_{\text{gal}} [h^3 \text{ Mpc}^{-3}]$	$z = 0$	$z = 0.5$	$z = 1$
10^{-2}	94.6%	94.3%	94.1%
10^{-3}	94.3%	93.8%	93.2%
10^{-4}	93.4%	92.5%	91.7%

matching rates are summarized in Table A2. The M_{prog} model can select more than 90% of subhalos which are selected by the V_{peak} model by taking a certain z_{prog} value. Thus the M_{prog} model can mimic the V_{peak} model in predicting galaxy clustering.

This paper has been typeset from a $\text{TeX}/\text{L}\ddot{\text{A}}\text{TeX}$ file prepared by the author.